Euclid: Searching for pair-instability supernovae with the Deep Survey

Euclid Collaboration

2022-10-20

Euclid: Searching for pair-instability supernovae with the Deep Survey[★]

T. J. Moriya[1,2,★★], C. Inserra[3], M. Tanaka[4,5], E. Cappellaro[6], M. Della Valle[7,8,9], I. Hook[10], R. Kotak[11], G. Longo[12,8],
F. Mannucci[13], S. Mattila[11], C. Tao[14], B. Altieri[15], A. Amara[16], N. Auricchio[17], D. Bonino[18], E. Branchini[19,20],
M. Brescia[7], J. Brinchmann[21], S. Camera[22,23,18], V. Capobianco[18], C. Carbone[24], J. Carretero[25,26], M. Castellano[27],
S. Cavuoti[7,8,12], A. Cimatti[28,13], R. Cledassou[29,30], G. Congedo[31], C. J. Conselice[32], L. Conversi[33,15], Y. Copin[34],
L. Corcione[18], F. Courbin[35], M. Cropper[36], A. Da Silva[37,38], H. Degaudenzi[39], M. Douspis[40], F. Dubath[39],
C. A. J. Duncan[41,32], X. Dupac[15], S. Dusini[42], A. Ealet[34], S. Farrens[43], S. Ferriol[34], M. Frailis[44], E. Franceschi[17],
M. Fumana[24], B. Garilli[24], W. Gillard[14], B. Gillis[31], C. Giocoli[45,46], A. Grazian[6], F. Grupp[47,48], S. V. H. Haugan[49],
W. Holmes[50], F. Hormuth[51], A. Hornstrup[52], K. Jahnke[53], S. Kermiche[14], A. Kiessling[50], M. Kilbinger[43],
T. Kitching[36], H. Kurki-Suonio[54], S. Ligori[18], P. B. Lilje[49], I. Lloro[55], E. Maiorano[17], O. Mansutti[44], O. Marggraf[56],
K. Markovic[50], F. Marulli[28,17,57], R. Massey[58], H. J. McCracken[59], M. Melchior[60], M. Meneghetti[17,57], G. Meylan[35],
M. Moresco[28,17], L. Moscardini[28,17,57], E. Munari[44], S. M. Niemi[61], C. Padilla[26], S. Paltani[39], F. Pasian[44],
K. Pedersen[62], V. Pettorino[43], M. Poncet[30], L. Popa[63], F. Raison[47], J. Rhodes[50], G. Riccio[7], E. Rossetti[28],
R. Saglia[47,48], B. Sartoris[44,64], P. Schneider[56], A. Secroun[14], G. Seidel[53], C. Sirignano[65,42], G. Sirri[57], L. Stanco[42],
P. Tallada-Crespí[66,25], A. N. Taylor[31], I. Tereno[37,67], R. Toledo-Moreo[68], F. Torradeflot[66,25], Y. Wang[69],
G. Zamorani[17], J. Zoubian[14], S. Andreon[70], V. Scottez[59,71], and P. W. Morris[72]

(Affiliations can be found after the references)

ABSTRACT

Pair-instability supernovae are theorized supernovae that have not yet been observationally confirmed. They are predicted to exist in low-metallicity environments. Because overall metallicity becomes lower at higher redshifts, deep near-infrared transient surveys probing high-redshift supernovae are suitable to discover pair-instability supernovae. The *Euclid* satellite, which is planned launch in 2023, has a near-infrared wide-field instrument that is suitable for a high-redshift supernova survey. The Euclid Deep Survey is planned to make regular observations of three Euclid Deep Fields (40 deg² in total) spanning *Euclid*'s six-year primary mission period. While the observations of the Euclid Deep Fields are not frequent, we show that the predicted long duration of pair-instability supernovae would allow us to search for high-redshift pair-instability supernovae with the Euclid Deep Survey. Based on the current observational plan of the *Euclid* mission, we conduct survey simulations in order to estimate the expected numbers of pair-instability supernova discoveries. We find that up to several hundred pair-instability supernovae at $z \lesssim 3.5$ can be discovered within the Euclid Deep Survey. We also show that pair-instability supernova candidates can be efficiently identified by their duration and color, which can be determined with the current Euclid Deep Survey plan. We conclude that the *Euclid* mission can lead to the first confirmation of pair-instability supernovae if their event rates are as high as those predicted by recent theoretical studies. We also update the expected numbers of superluminous supernova discoveries in the Euclid Deep Survey based on the latest observational plan.

Key words. stars: massive – supernovae: general – surveys

1. Introduction

Optical transient surveys have revealed the existence of huge diversity in supernovae (SNe), and many new kinds of SNe that were not recognized before have been discovered (Inserra 2019). For example, SNe that are often more than ten times more luminous than other SNe, known as superluminous SNe (SLSNe; see Gal-Yam 2019 for a recent review), were discovered through unbiased optical transient surveys (Quimby et al. 2011). Just after the existence of SLSNe was recognized, they were often theoretically linked to pair-instability SNe (PISNe; e.g., Smith et al. 2007; Gal-Yam et al. 2009). PISNe are theorized thermonuclear explosions of very massive stars

(Barkat et al. 1967; Rakavy & Shaviv 1967) with a helium core mass between $\simeq 65\,M_\odot$ and $\simeq 135\,M_\odot$ (e.g., Heger & Woosley 2002). Some PISNe are predicted to produce a large amount of radioactive ^{56}Ni, up to $\simeq 60\,M_\odot$, which heats SN ejecta, and they can be as bright as SLSNe (Kasen et al. 2011; Dessart et al. 2013; Gilmer et al. 2017). However, the light-curve and spectral properties of SLSNe are now found to be different from those predicted for PISNe (e.g., Dessart et al. 2012; Nicholl et al. 2013; Jerkstrand et al. 2016; Inserra et al. 2017; Mazzali et al. 2019). Therefore, it is generally believed that most SLSNe are not PISNe and that they are powered by a different mechanism (see Moriya et al. 2018 for a review on SLSN powering mechanisms). No SNe have been confirmed to be PISNe to date, although there are several possible PISN candidates (e.g., Lunnan et al. 2016; Terreran et al. 2017) and some possible indirect signatures of PISNe (e.g., Aoki et al. 2014; Isobe et al. 2022). Confirming the existence of PISNe is a critical test of

---

Table 1. List of SN templates used in this study.

Name	Explosion	Progenitor	Mass
R250 [a]	PISN	RSG	250 $M_\odot$
R225 [a]	PISN	RSG	225 $M_\odot$
R200 [a]	PISN	RSG	200 $M_\odot$
R175 [a]	PISN	RSG	175 $M_\odot$
R150 [a]	PISN	RSG	150 $M_\odot$
He130 [a]	PISN	WR	130 $M_\odot$
He120 [a]	PISN	WR	120 $M_\odot$
He110 [a]	PISN	WR	110 $M_\odot$
He100 [a]	PISN	WR	100 $M_\odot$
He090 [a]	PISN	WR	90 $M_\odot$
SLSN [b]	SLSN	–	–

Notes. [a]Kasen et al. (2011). [b]Moriya et al. (2022).

stellar evolution theory (Langer 2012). PISNe can play an important role in chemical evolution (e.g., Nomoto et al. 2013). PISNe are also essential components for the proper understanding of black hole mass distributions observed by gravitational waves (e.g., Marchant et al. 2016; Farmer et al. 2019).

Pair-instability SNe are believed to appear in low-metallicity environments below $Z_\odot/3$ (Langer et al. 2007, but see also Georgy et al. 2017). Thus, they may preferentially appear at high redshifts where metallicity is low (e.g., Chruslinska & Nelemans 2019). However, it is difficult to discover high-redshift PISNe with optical transient surveys as they become faint in the optical wavelength range because of redshift. For example, a deep optical transient survey with Subaru/Hyper Suprime-Cam (HSC) carried out a search for high-redshift PISN candidates, but no candidates have been found so far (Moriya et al. 2021). The future *Vera C. Rubin* Observatory/Legacy Survey of Space and Time (LSST) may be able to discover PISNe depending on its survey strategy that has not yet been determined (e.g., du Buisson et al. 2020). A deep transient survey in the near-infrared (NIR) is observationally better suited to discover PISNe appearing at high redshifts (Scannapieco et al. 2005; Pan et al. 2012; Whalen et al. 2013; Moriya et al. 2019, 2022; Wong et al. 2019; Regős et al. 2020).

There are several wide-field NIR instruments planned for the 2020s such as the Wide Field Instrument on *Nancy Grace Roman* Space Telescope from 2026 (Spergel et al. 2015) and the ULTIMATE Wide Field Instrument on Subaru from 2027[1]. Among them, *Euclid* is planned to be launched in 2023 (Laureijs et al. 2011). It has wide-field (0.53 deg^2) imagers, one in the visual range (with a passband that we denote I_E) and the other in the NIR range with three filters (Y_E, J_E, and H_E). The *Euclid* mission plans wide (15 000 deg^2) and deep (40 deg^2) surveys in the four filters (Euclid Collaboration 2022a). As introduced below, the Euclid Deep Survey (EDS) covering 40 deg^2 in total is planned to visit the survey fields regularly during the six-year primary survey period of the *Euclid* mission (Laureijs et al. 2011; Euclid Collaboration 2022a). Although the current EDS plan is not suitable for searching for short-duration Type Ia SNe (SNe Ia, Astier et al. 2014), Inserra et al. (2018a) previously showed that the regular observations planned in EDS allow us to search for high-redshift SLSNe up to $z \simeq 3.5$.

High-redshift PISNe are expected to be bright in the NIR and have long durations (Sect. 2.1). Therefore, it is possible

that high-redshift PISNe can be identified even with the long cadence observations planned in EDS (Sect. 3.1). In this work, we performed transient survey simulations in order to quantify the expected numbers of PISN discoveries in EDS. We also investigated the expected numbers of SLSN discoveries in EDS, because the EDS observational plan has been updated since the publication of Inserra et al. (2018a).

The rest of this paper is organized as follows. We first introduce the light-curve templates of PISNe and SLSNe we used in our survey simulations in Sect. 2. We then introduce the assumptions in our survey simulations in Sect. 3. The survey simulation results are presented in Sect. 4. We discuss how to identify high-redshift PISN and SLSN candidates efficiently with photometry in Sect. 5. Section 6 concludes this paper. All magnitudes presented in this paper are in the AB system. We adopt the ΛCDM cosmology with $H_0 = 70$ km s^{-1} Mpc^{-1}, $\Omega_\Lambda = 0.7$, and $\Omega_m = 0.3$.

2. SN templates

SN templates are required to estimate the observational properties at high redshifts. The SN templates we used in this study are introduced in this section. They are summarized in Table 1.

2.1. PISNe

We used the synthetic spectral evolution of PISNe obtained by Kasen et al. (2011), who took the PISN explosion models from Heger & Woosley (2002) and calculated their spectral evolution by performing radiative transfer calculations. Kasen et al. (2011) calculated PISN properties for red supergiant (RSG), blue supergiant (BSG), and Wolf-Rayet (WR) progenitors. The RSG and BSG PISN progenitors have hydrogen-rich envelopes, while WR PISN progenitors are hydrogen-free. The BSG PISN progenitors are expected to exist mainly at zero metallicity (Heger & Woosley 2002). The highest redshift PISNe that can be discovered by the *Euclid* survey, which is determined by the maximum expected luminosity of PISNe, is $z \simeq 3.5$ as we show later and most of them are not likely to have zero metallicity. Thus, a significant fraction of PISNe discovered by *Euclid* would be from RSG and WR progenitors, and we adopted RSG and WR PISN models in this study. The RSG PISN models have a metallicity of $10^{-4} Z_\odot$. Although the metallicity of the host galaxies in the redshift range we can probe with EDS is higher than $10^{-4} Z_\odot$ (e.g., Steidel et al. 2014; Chruslinska & Nelemans 2019), their light-curve properties are not significantly different from those with high metallicity (e.g., Kozyreva et al. 2014). We also take PISNe with WR progenitors into account in this study. The WR PISN models in Kasen et al. (2011) were calculated with the zero-metallicity condition (Heger & Woosley 2002), but WR PISNe can appear with finite metallicity (e.g., du Buisson et al. 2020). The light-curve properties of zero-metallicity WR PISN models are not significantly different from those of higher metallicity WR PISNe up to the proposed PISN metallicity threshold of around $Z_\odot/3$ (Moriya et al., in prep.). Thus, we adopted the WR PISN properties from the zero metallicity progenitors in this study. We note that the adopted progenitor models do not take stellar rotation into account (e.g., Chatzopoulos & Wheeler 2012). In addition, only the wind mass loss is considered.

Kasen et al. (2011) provide the RSG PISN explosion models for 250 $M_\odot$ (R250), 225 $M_\odot$ (R225), 200 $M_\odot$ (R200), 175 $M_\odot$ (R175), and 150 $M_\odot$ (R150) stars at the zero-age main sequence, and we investigated them all. We adopted the WR PISN models whose progenitor evolution is calculated from the helium

---

[1] https://ultimate.naoj.org/
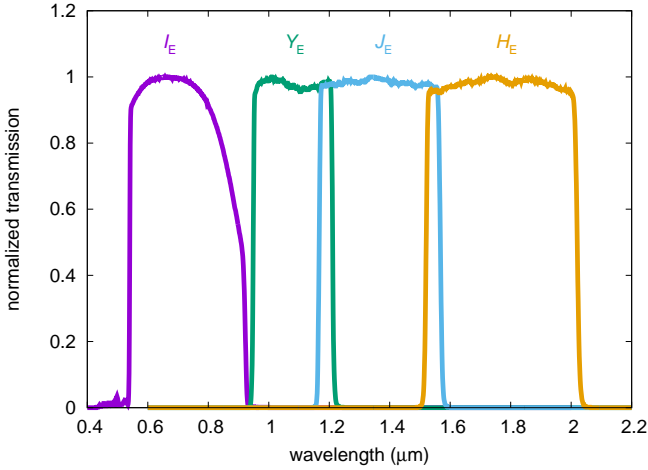
Fig. 1. Normalized *Euclid* filter transmission (Euclid Collaboration 2022a,b).
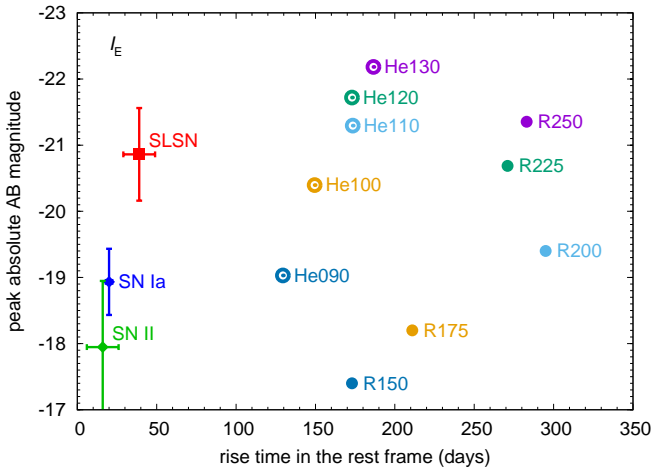
Fig. 2. Rise times and peak absolute magnitudes of the PISN and SLSN models in the rest frame in the I_E band. The PISN models (R250, R225, R200, R175, R150, He130, He120, He110, He100, and He090) are from Kasen et al. (2011) and the SLSN template is from Moriya et al. (2022). We also show rise times and peak absolute magnitudes of the SN Ia template from Hsiao et al. (2007) and the SN II Nugent template for comparison (see Sect. 5 for details). The error bars in the SLSN, SN Ia, and SN II templates show a typical dispersion (e.g., Richardson et al. 2014; Miller et al. 2020; González-Gaitán et al. 2015).

zero-age main sequence with a helium core mass of $130\,M_\odot$ (He130), $120\,M_\odot$ (He120), $110\,M_\odot$ (He110), $100\,M_\odot$ (He100), and $90\,M_\odot$ (He090). They are the five brightest WR PISNe presented in Kasen et al. (2011), whereas the WR PISN models below $90\,M_\odot$ are too faint to be observed in our redshift range of interest (see Sect. 3.1).

In order to estimate the PISN properties at high redshifts, we took the rest-frame synthetic spectra, shifted them to an assumed redshift, and convolved the shifted observer-frame spectra with the *Euclid* filter transmission (Fig. 1). The rise times and peak absolute magnitudes of the PISN models in the rest frame are summarized in Fig. 2. Figure 3 shows the H_E-band light curves of the brightest RSG PISN model (R250) and the brightest WR PISN model (He130) at $z = 2$ and 3. Figure 4 shows the peak magnitudes of the PISN models at $0.5 < z < 4$ within the four *Euclid* filters.
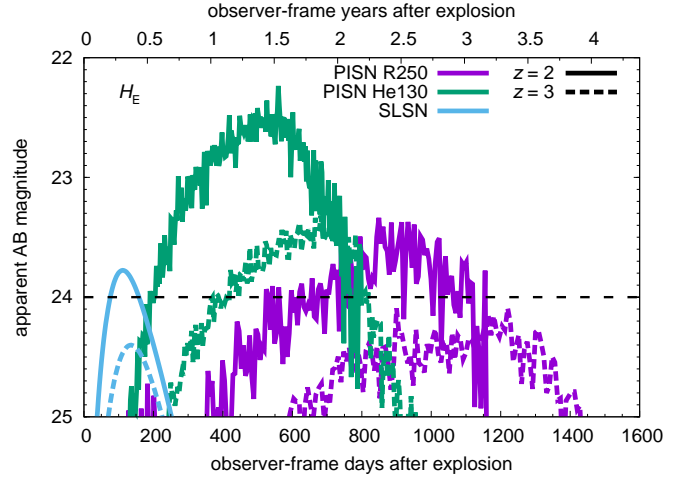
Fig. 3. H_E-band light curves of the R250 PISN model, the He130 PISN model, and the SLSN template at $z = 2$ and 3. The horizontal dashed line at $H_E = 24.0$ mag shows the 5σ limiting magnitude of each visit planned in the EDS observations.

We did not consider Lyα absorption by the intergalactic medium (IGM) and circumgalactic medium (CGM) in this study. The IGM and CGM absorption affect the brightness in the I_E band for SNe mainly at $z \gtrsim 3$. PISNe at $z \gtrsim 3$ are fainter than the I_E-band detection limit (25.5 mag) except for the R250 PISN model (Fig. 4). In addition, the maximum redshift up to which we can discover R250 PISNe with the assumed cadence is estimated to be $z \simeq 2.5$, as shown in the following sections. Thus, the Lyα absorption does not affect our conclusions in this study.

2.2. SLSNe

In this study, we only considered hydrogen-poor (Type I) SLSNe as in our previous study (Inserra et al. 2018a), and we refer to hydrogen-poor SLSNe simply as SLSNe. This is because the observational properties of nearby hydrogen-poor SLSNe have been thoroughly investigated and we can reliably estimate their high-redshift properties. Contrarily, hydrogen-rich (Type II) SLSNe are known to exist (e.g., Smith et al. 2007; Inserra et al. 2018b), but their rest-frame ultraviolet properties have not been studied well enough to estimate their high-redshift properties.

We used the SLSN template presented in Moriya et al. (2022). The SLSN spectral template was constructed by assuming a broken blackbody function as originally introduced by Prajs et al. (2017). The template spectra above 300 nm follow the blackbody function as observed in SLSNe (e.g., Quimby et al. 2018). Below 300 nm, the blackbody function is truncated to match the spectral shape of the well-observed SLSN iPTF13ajg (Vreeswijk et al. 2014). iPTF13ajg has the typical shape of SLSN ultraviolet spectra at around peak luminosity, although some SLSNe are known to be brighter in the ultraviolet (Nicholl et al. 2017). We only take the spectral shape of iPTF13ajg, and the template peak luminosity is adjusted to match an average value. The template has a peak u-band absolute magnitude of -21.1 mag, which is an average SLSN peak brightness estimated by Lunnan et al. (2018). The u-band light-curve rise time of the template is 30 days.

The rise time and peak absolute magnitude of the SLSN template in the rest frame are compared to those of the PISN models in Fig. 2. The peak observer-frame magnitudes of the SLSN
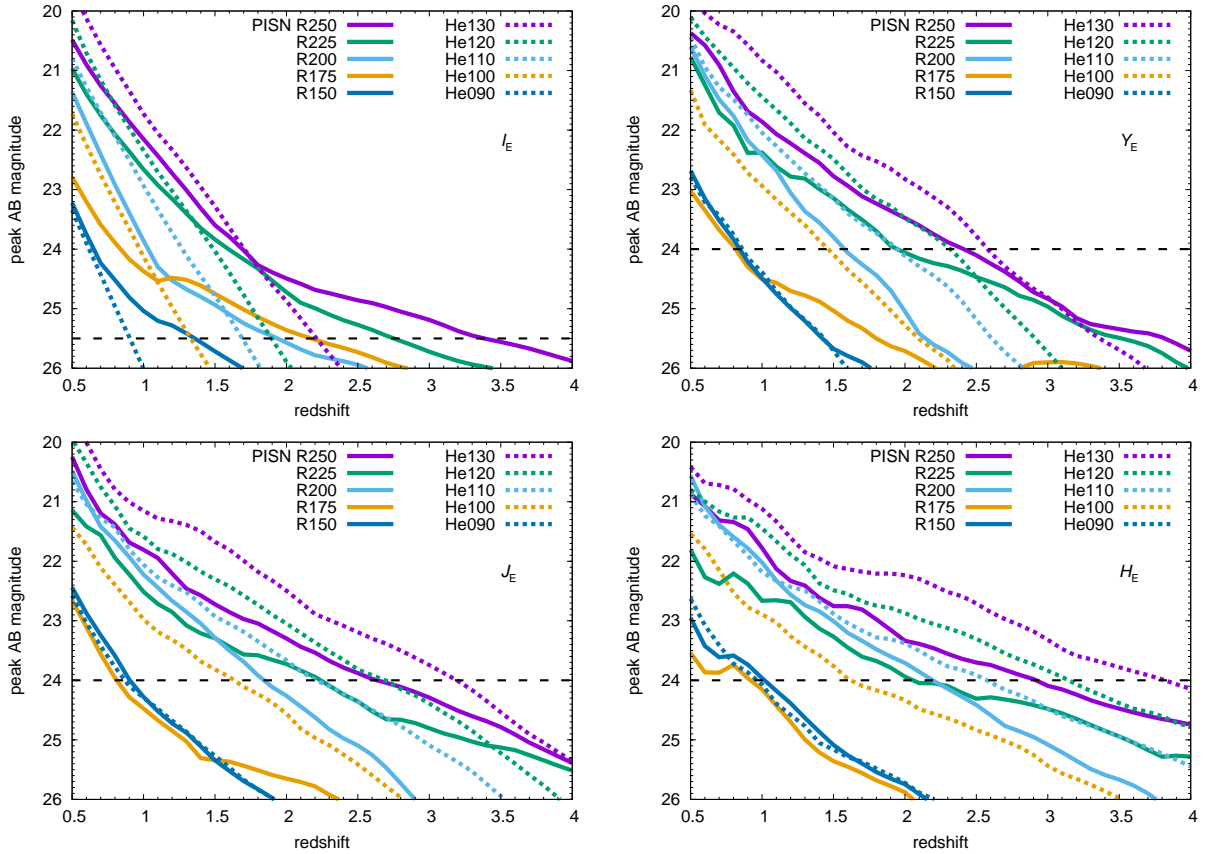
Fig. 4. Peak magnitudes of PISN models. The point-source 5σ limiting magnitudes of each visit adopted in our survey simulations (25.5 mag for the I_E band and 24.0 mag for the Y_E, J_E, and H_E bands in AB magnitudes) are shown with the dashed lines. As discussed in Sect. 3.1, *Euclid* may actually have slightly better limiting magnitudes.

template at $0.5 < z < 4$ obtained by convolving the *Euclid* filters are presented in Fig. 5. In the following survey simulations, the peak SLSN magnitudes are assumed to randomly scatter from the average value by a standard deviation of 0.7 mag with a Gaussian probability distribution in order to account for the SLSN luminosity diversity (Lunnan et al. 2018). While the actual luminosity function of SLSNe may not have a Gaussian distribution function (e.g., De Cia et al. 2018; Perley et al. 2020), a Gaussian distribution with 0.7 mag standard deviation covers the wide peak luminosity range observed in SLSNe. Similarly, the rise times are independently set to have a standard deviation of ten days with a Gaussian probability distribution, but the rise times are not allowed to be shorter than ten days. As mentioned in Sect. 2.1, no Lyα absorption in the IGM and CGM is taken into account because no SLSNe at $z \gtrsim 3$ are brighter than the detection limit.
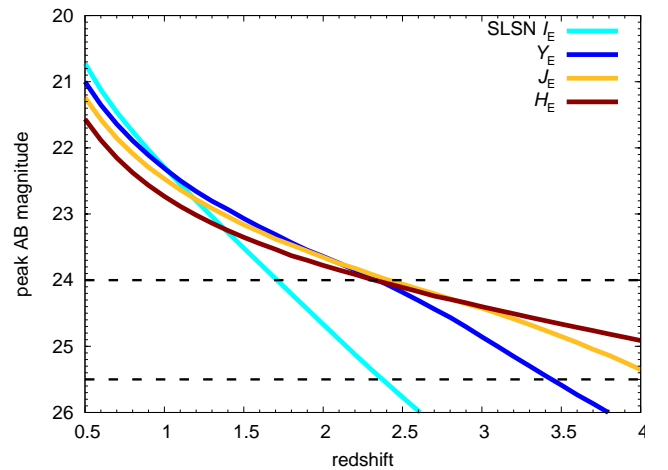
3. Survey simulation setups

In this section, we summarize the assumptions in our survey simulations.

3.1. Euclid Deep Fields, cadence, and sensitivity

The EDS will cover three Euclid Deep Fields (EDFs)[2]. Two fields are planned at the north and south ecliptic poles (EDFN

Fig. 5. Peak magnitudes of SLSN template. The limiting magnitudes of each visit by the EDS observations (25.5 mag for the I_E band and 24.0 mag for the Y_E, J_E, and H_E bands in AB magnitudes) are shown with the dashed lines. The template magnitudes are randomly scattered by the standard deviation of 0.7 mag (both to brighter and fainter magnitudes) assuming the Gaussian probability distribution in the survey simulations to match the observed luminosity function as discussed in Sect. 3.

and EDFS, respectively). The third field is in the *Chandra* Deep Field South located in Fornax (EDFF). We introduce the current
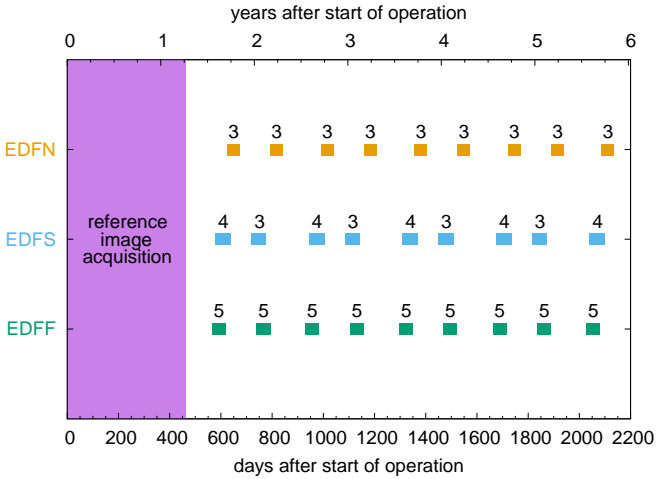
Fig. 6. EDF observation plan of *Euclid* mission (Euclid Collaboration 2022a). The date is from the beginning of *Euclid* operation. The observational epochs at each EDF are shown with squares. The numbers above the squares show the number of visits within each epoch. For example, five visits for the entire 10 deg² of EDFF will be made at every epoch shown with squares. The visits within one epoch are made within 15 days. We assume that the images taken in the first 1.25 yr of the mission are used to construct the reference images and the SN search starts after 1.25 yr.

observational plan at each field in this section, and this is also available in Euclid Collaboration (2022a).

EDFN will cover 10 deg² and will be visited ten times at the beginning of the *Euclid* mission for calibration purposes. Then, it will be observed regularly roughly every six months during the six-year primary mission period. EDFS will cover 20 deg² and the whole field will be visited 45 times. The first ten visits will be done at the beginning of the mission, and then the subsequent 35 visits will span five years. Finally, the 10 deg² area in EDFF will be observed 56 times in total over six years.

Figure 6 summarizes the current observational plan for the EDFs. The observations at each EDF will be conducted at the epochs indicated by squares. The numbers above show the number of visits planned in each epoch. For example, five visits are planned for EDFF for the entire 10 deg² area in every epoch shown with the squares. The visits within each epoch are done within 15 days. The brightness of high-redshift PISNe does not change significantly in 15 days (Fig. 3), and thus for PISNe we regard each square containing several visits as one epoch. At each visit, images in the I_E, Y_E, J_E, and H_E filters will be taken covering the entire survey field. The 5σ limiting magnitudes of each visit are estimated to be $I_E = 25.5$ mag and $Y_E = J_E = H_E = 24.0$ mag in Inserra et al. (2018a), and we adopted these limiting magnitudes in this study. For example, five visits are planned for EDFF with the above 5σ limiting magnitudes in each epoch. We note that the recently updated estimates for the limiting magnitudes are better than those we used in this study (Euclid Collaboration 2022a; Guy et al. 2021). In addition, the limiting magnitudes are for each visit. Because we have multiple visits in one epoch, we can obtain slightly deeper images by stacking all visits in one epoch. Meanwhile, when we perform image subtraction for transient identification, noise will increase and the detection limits can be reduced. The noise due to image subtraction may not be significant thanks to stable *Euclid* point spread functions, although the diffraction-limited NIR point spread functions are under-sampled. The actual lim-

iting magnitudes will be revealed when the *Euclid* observations start.

As shown in Fig. 6, the EDFs will be repeatedly observed with about a half-year separation. The high-redshift PISNe are expected to be brighter than 24.0 mag in the NIR bands for a year or more (Fig. 3). Thus, the planned six-monthly observations are suitable for searching for high-redshift PISNe. On the other hand, the typical duration of high-redshift SLSNe is not long enough for them to be captured by the half-year cadence. However, they can be still identified because there are multiple (3–5) visits made in a single epoch. We note that the EDS observation plan has been updated since the previous study of Inserra et al. (2018a). Some EDFs were planned to have more frequent visits in the previous plan, which was therefore more suitable for SLSN discovery.

In order to discover transients on the sky, deep reference images are required. We assume that deep reference images are created using images taken during the first 1.25 yr of the *Euclid* mission, as indicated in Fig. 6. Many calibration visits are planned in the first year covering the three EDFs. The EDFs will be observed 7–13 times, depending on the field, in the first 1.25 yr (Euclid Collaboration 2022a), and this number of observations is enough to create reference images of sufficient depth for subtraction.

3.2. Event rates

Event rates are an essential assumption in the transient survey simulations. Because no confident PISNe have been discovered so far, the PISN event rate is unknown. Observationally, the PISN event rate is constrained to be less than the SLSN event rate (e.g., Nicholl et al. 2013; Moriya et al. 2021). The SLSN event rate and its redshift evolution have been constrained by optical transient surveys (Quimby et al. 2013; Prajs et al. 2017; Frohmaier et al. 2021). The SLSN event rate at $z \simeq 0.2$ is estimated to be 30 Gpc⁻³ yr⁻¹ (Quimby et al. 2013). The SLSN event rate up to $z \simeq 1$ is estimated to be consistent with that obtained by extrapolating the $z \simeq 0.2$ rate following the cosmic star-formation rate (SFR) density of Madau & Dickinson (2014, Fig. 7). We currently have a few possible PISN candidates, as discussed in Sect. 1. The total number of SLSN discoveries is currently around 100–200 (e.g., Nicholl 2021; Chen et al. 2022a,b). Although it is likely inappropriate to compare the numbers of the PISN candidates and the SLSN discoveries because of their different properties especially in spectral energy distributions (Sect. 2), the current fraction of PISN candidates to SLSNe should be around a few per cent.

Theoretical predictions for the PISN rates are also very different (see Langer et al. 2007; Magg et al. 2016; Takahashi 2018; Farmer et al. 2019; du Buisson et al. 2020; Tanikawa et al. 2022). If we simply assume a Salpeter initial mass function and a PISN mass range of 150–300 $M_\odot$ (Heger & Woosley 2002), 1% of core-collapse SNe (8–25 $M_\odot$) would be PISNe. Given core-collapse SN rates of 10^5–10^6 Gpc⁻³ yr⁻¹ at $z = 0$–2.5 (Strolger et al. 2015), the corresponding PISN rate is 10^3–10^4 Gpc⁻³ yr⁻¹, which is much higher than the aforementioned SLSN rate. Recently, Briel et al. (2022) provided theoretical predictions for the PISN rates. By using several cosmic SFR densities from both observations and cosmological simulations, they predicted PISN rates based on stellar evolution models from Binary Population and Spectral Synthesis (BPASS, Eldridge et al. 2017; Stanway & Eldridge 2018). The PISN rate predictions at $z \lesssim 3.5$ are shown to be 10–100% of the SLSN rate (Fig. 7).
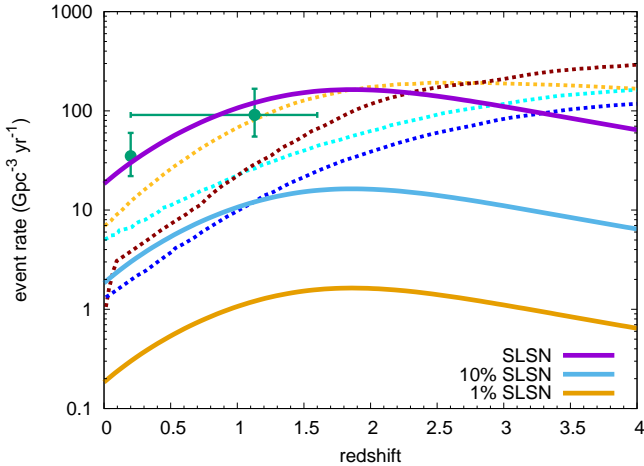
Fig. 7. Event rates used in survey simulations. The SLSN event rate is estimated by setting the SLSN event rate at $z = 0.2$ to be $30\,\mathrm{Gpc^{-3}\,yr^{-1}}$ (Quimby et al. 2013; Frohmaier et al. 2021) and extrapolating it following the cosmic SFR density of Madau & Dickinson (2014). For reference, the SLSN rates constrained by observations at $z \sim 0.2$ (Frohmaier et al. 2021) and $z \sim 1.1$ (Prajs et al. 2017) are shown. We also used the 10% and 1% SLSN rates for PISNe. Four theoretical PISN rate estimates by Briel et al. (2022, dotted lines) are shown for comparison. The four models have different assumptions on the cosmic SFR history.

Although the PISN event rate is unknown, we need to assume some PISN event rates for our survey simulations. We think it is reasonable to assume PISN rates that are scaled with the SLSN event rate for our purpose. The SLSN event rate is constrained observationally, and we do not need to rely on uncertain theoretical rate predictions in this way. A fraction of SLSNe may be PISNe, even though we do not have a conclusive case. In addition, the latest theoretical study by Briel et al. (2022) predicts that the PISN rate at $z \lesssim 3.5$ is 10–100% of the SLSN rate (Fig. 7). In light of the above and given the large uncertainties involved in this type of estimate, we make three assumptions for the PISN event rate: it is (i) the same as the SLSN event rate, (ii) 10% of the SLSN event rate, and (iii) 1% of the SLSN event rate.

NIR and radio surveys for core-collapse SNe in the local Universe have shown that a significant fraction of the events are lost from current optical surveys as they explode in very dusty environments (e.g., Mannucci et al. 2007; Pérez-Torres et al. 2009; Mattila et al. 2012; Kool et al. 2018; Jencson et al. 2019; Kankare et al. 2021; Fox et al. 2021). In particular, the fraction of star-formation activity that takes place in luminous starbursting and dusty galaxies increases sharply with redshift and becomes the dominant component of star formation at $z \simeq 1$. Consequently, an increasing fraction of SNe are expected to be lost from high-redshift optical searches. Up to 60% of core-collapse SNe are likely to be lost at $z \simeq 2$ (Mannucci et al. 2007). Since the SLSN rates discussed in this section are based on optical surveys, the rates extrapolated to $z \simeq 4$ should be taken with some caution. They can probably be considered as lower limits to the actual event rate.

3.3. Discovery criteria

PISNe and SLSNe are assumed to appear randomly following the assumed event rates in the survey simulations. Once a PISN or SLSN appears, the expected magnitudes in each epoch are

estimated for the event. If it satisfies the discovery criteria presented below, the event is regarded as a discovery.

High-redshift PISNe remain bright for a year or more (Fig. 3), while other common high-redshift SNe such as SNe Ia do not remain bright for a long (Hounsell et al. 2018), as can be seen in Fig. 2. Thus, the transient duration is important information to identify rare high-redshift PISNe among many other kinds of high-redshift SNe. We therefore count the numbers of PISNe that become brighter than the limiting magnitude for two epochs or more in any band in our survey simulations. We also investigate the PISN candidate selection through their color in Sect. 5. Even if we have a detection only in a single band, non-detection in the other bands can constrain the color of SN candidates.

High-redshift SLSNe usually have shorter durations than those of PISNe (Figs. 2 and 3) and it is difficult to distinguish them from other high-redshift SNe by duration with the current EDS plan having a cadence of about a half year (Fig. 6). However, high-redshift SLSNe can be identified among other short-duration SNe by their color even with a single epoch when they are brighter than 24 mag in the NIR bands (Sect. 5). We count the number of SLSNe that become brighter than the detection limit at the first visit of each epoch in any band, although many other short-duration SNe will be detected with this criterion (Sect. 5). For comparison, we also show the number of SLSNe that exceed the detection limits for two epochs.

4. Simulation results

Survey simulations with one set of assumptions are performed 10^3 times, and we obtain the average numbers of discoveries. The survey simulations are performed in the three EDFs independently, with their areas and cadences as discussed in Sect. 3.1. However, there are no significant differences in the redshift distributions of the discovered PISNe and SLSNe among the three EDFs. Therefore, we show and discuss the combined numbers of PISN and SLSN discoveries in the three fields. The total numbers of PISN and SLSN discoveries in the three EDFs are summarized in Table 2.

Figure 8 shows the cumulative redshift distributions of PISNe discovered in our survey simulations. We show the distributions for the three different assumptions for the event rates of the PISN models (100%, 10%, and 1% of the SLSN rate), and the expected discovery numbers are roughly proportional to the assumed rate. The brightest PISN models such as R250 and He130 can be discovered with EDS if their rates are more than about 1% of the SLSN rate. Meanwhile, the faintest PISN models in our survey simulations such as R150 and He090 can only be discovered if their event rates are as high as those of SLSNe. Figure 9 shows the redshift distributions of the discovered PISNe for the same event rates as the SLSN event rate. The shapes of the redshift distributions do not depend on the assumed rate. The brightest PISN model He130 can be discovered up to $z \simeq 3.5$. The brightest RSG PISN models (R250 and R225) can be discovered up to $z \simeq 2.5$. The faintest PISN models (R150 and He090) can be discovered only up to $z \simeq 0.6$–0.8 and, therefore, their expected discovery numbers are relatively small.

The expected cumulative number distributions for SLSNe are presented in Fig. 10 and their number density distributions are shown in Fig. 9. As discussed previously, the durations of high-redshift SLSNe are much shorter than those of PISNe. Figure 11 shows the distribution of the number of detection epochs in our survey simulations. Only about 20% of high-redshift SLSNe can be identified if we require them to

Table 2. Expected numbers of PISN and SLSN discoveries with EDS.

Model	Rate [a]	Detection [b] (epochs)	Total	Redshift range							
				0–0.5	0.5–1.0	1.0–1.5	1.5–2.0	2.0–2.5	2.5–3.0	3.0–3.5	3.5–4.0
R250	1	2	145	4.5	25	47	49	19	0.030	0	0
R250	0.1	2	14	0.46	2.5	4.7	4.9	1.9	0.0030	0	0
R250	0.01	2	1.5	0.045	0.27	0.52	0.49	0.19	0.0010	0	0
R225	1	2	158	4.4	25	47	53	28	0	0	0
R225	0.1	2	16	0.46	2.6	4.8	5.2	2.7	0	0	0
R225	0.01	2	1.6	0.036	0.25	0.43	0.54	0.29	0	0	0
R200	1	2	49	4.4	23	21	0	0	0	0	0
R200	0.1	2	4.9	0.47	2.4	2.1	0	0	0	0	0
R200	0.01	2	0.52	0.056	0.24	0.23	0	0	0	0	0
R175	1	2	7.5	2.9	4.6	0	0	0	0	0	0
R175	0.1	2	0.79	0.29	0.49	0	0	0	0	0	0
R175	0.01	2	0.081	0.038	0.044	0	0	0	0	0	0
R150	1	2	3.2	1.5	1.7	0	0	0	0	0	0
R150	0.1	2	0.32	0.13	0.19	0	0	0	0	0	0
R150	0.01	2	0.033	0.018	0.015	0	0	0	0	0	0
He130	1	2	210	4.2	24	47	53	43	28	12	0.0060
He130	0.1	2	21	0.41	2.3	4.7	5.3	4.3	2.7	1.2	0
He130	0.01	2	2.1	0.040	0.26	0.46	0.51	0.45	0.26	0.12	0.00050
He120	1	2	164	4.3	21	47	51	36	3.8	0	0
He120	0.1	2	16	0.46	2.1	4.6	5.1	3.6	0.37	0	0
He120	0.01	2	1.6	0.048	0.20	0.43	0.47	0.38	0.037	0	0
He110	1	2	103	4.3	20	45	32	2.2	0	0	0
He110	0.1	2	10	0.43	2.1	4.5	3.2	0.24	0	0	0
He110	0.01	2	1.1	0.051	0.20	0.47	0.32	0.027	0	0	0
He100	1	2	25	4.1	16	4.7	0	0	0	0	0
He100	0.1	2	2.4	0.40	1.6	0.45	0	0	0	0	0
He100	0.01	2	0.24	0.049	0.16	0.038	0	0	0	0	0
He090	1	2	2.0	1.9	0.16	0	0	0	0	0	0
He090	0.1	2	0.20	0.18	0.024	0	0	0	0	0	0
He090	0.01	2	0.027	0.027	0	0	0	0	0	0	0
SLSN	1	2	28	2.6	8.5	8.9	5.1	2.1	0.75	0.25	0.096
SLSN	1	1	121	4.9	23	37	31	16	6.4	2.1	0.42

Notes. The total discovery numbers in the three EDFs are shown. [a] The event rate relative to the SLSN rate presented in Fig. 7. [b] The minimum number of detected epochs required to be regarded as a discovery.

be detected at multiple epochs. 28 SLSNe are expected to be detected at two epochs, while 121 SLSNe are discovered if SLSNe with only a single epoch detection are included. High-redshift SLSNe could be distinguished from high-redshift SNe Ia and II through color, as we discuss in Sect. 5. In addition, we have multiple visits at each epoch, and the luminosity evolution in individual visits can also be used to distinguish high-redshift SLSNe from high-redshift SNe Ia and II.

Although we lose a large fraction of high-redshift SLSNe if we take only those detected at multiple epochs, we still have 28 SLSNe with multiple epoch detection. Because of the unknown PISN rates, these SLSNe could be contaminants. The color of PISNe and SLSNe can be similar, and it is difficult to distinguish high-redshift PISNe and SLSNe by color alone (Sect. 5). Because almost no high-redshift SLSNe are expected to be detected at three epochs and many high-redshift PISNe can be brighter than the detection limits for three epochs, transients with three-epoch detection are likely to be genuine high-redshift PISN candidates.

Finally, no extinction is assumed in our survey simulations. The EDFs have little Galactic extinction, but the SNe could suffer from severe host galaxy extinction. However, PISNe and SLSNe preferentially appear in low-metallicity environments where little extinction is expected (Garn & Best 2010). Thus, overall, the effect of extinction may not be significant.

5. PISN and SLSN candidate identification with photometry
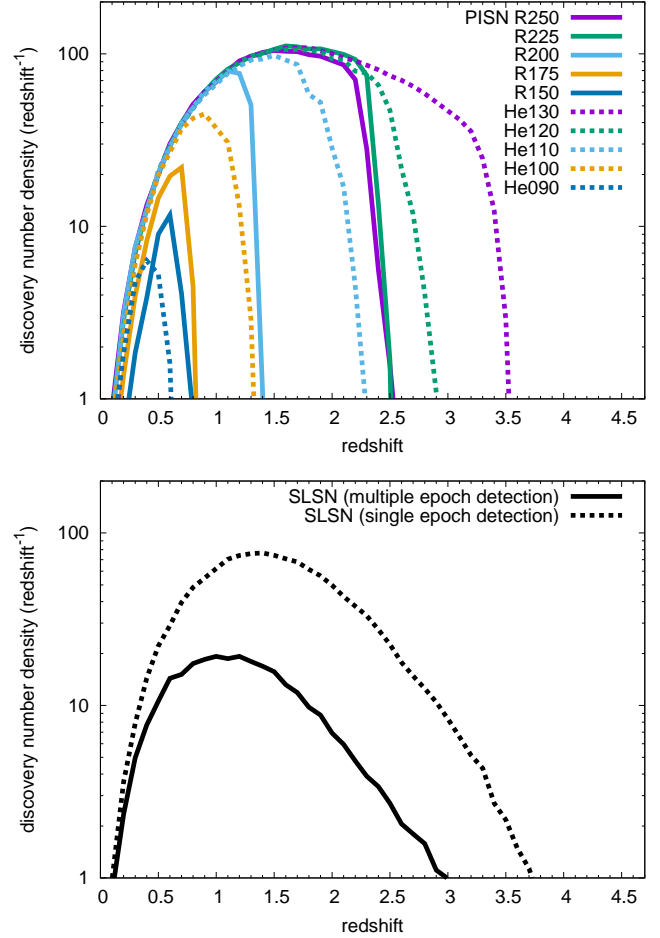
The efficient identification of rare PISN and SLSN candidates among many other abundant SNe such as SNe Ia is critical for triggering spectroscopic follow-up observations to confirm their discovery. The transient duration is an essential piece of information for identifying PISN candidates especially, as discussed in the previous section. Figure 11 clearly shows that most luminous PISNe are detected at more than two epochs, while other SNe are usually expected to be bright for one epoch with the half-year cadence observations. Still, it is important to have as much information as possible to screen the best PISN and SLSN candidates to make the best use of follow-up resources. In this section, we discuss the color of PISNe and SLSNe, which can be used to distinguish them from other common SNe.
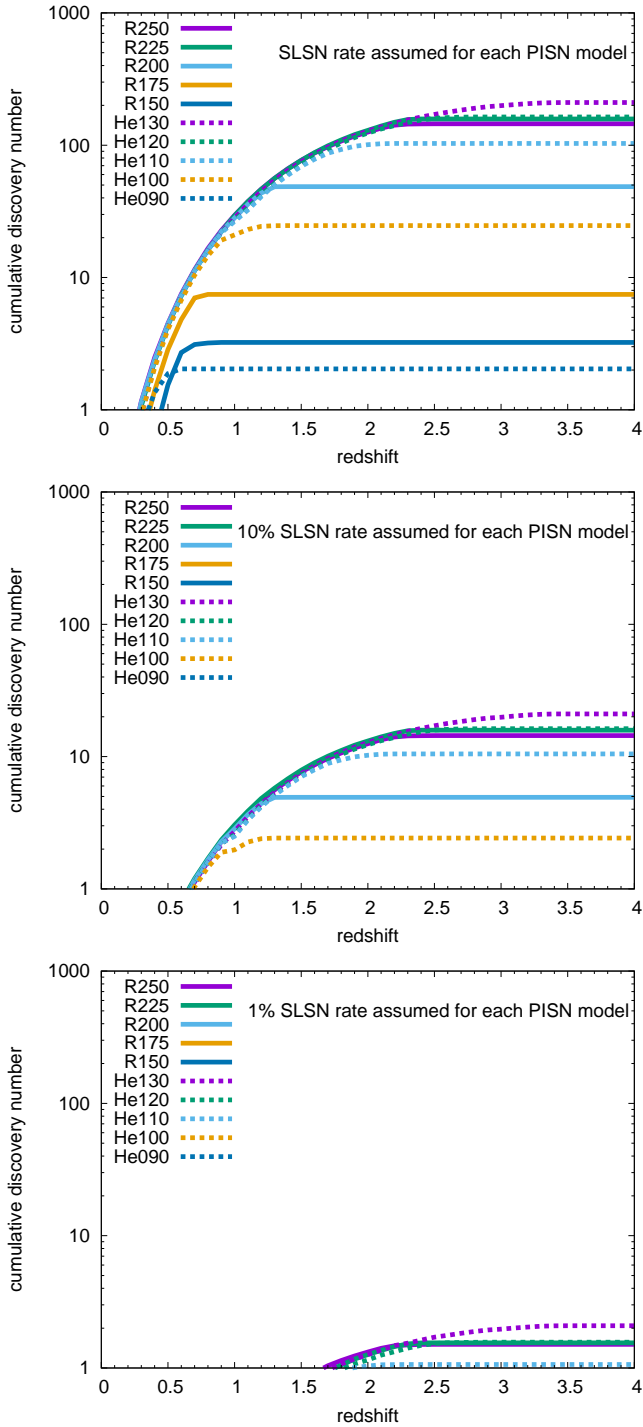
Fig. 8. Cumulative redshift distributions of PISNe discovered in survey simulations. The total discovery numbers in the three EDFs are presented. The *top*, *middle*, and *bottom* panels show the results for the event rates of 100%, 10%, and 1% of the SLSNe rate for each PISN model.
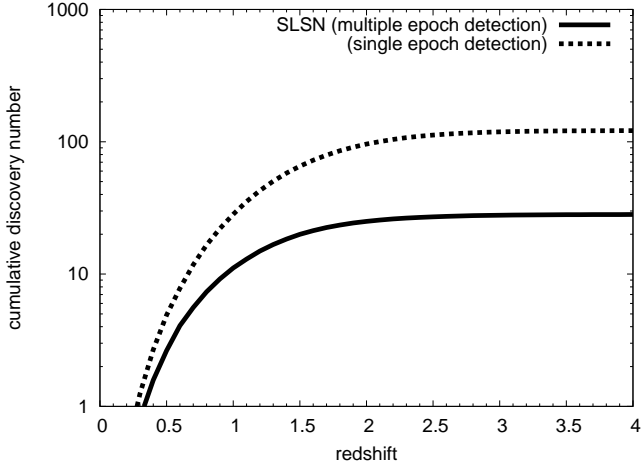

Fig. 9. Redshift distributions of PISNe (*top panel*) and SLSNe (*bottom panel*) discovered in the survey simulations. The total discovery numbers in the three EDFs are presented. The event rates are set to be the same as the SLSN rate in all the models in this figure, but the shape of the redshift distribution is not affected by the assumed rate.

Blanco/Dark Energy Camera, or the future *Vera C. Rubin* Observatory/LSST. A few SNe per square degree at $z < 0.5$ are likely to appear at each epoch (Yasuda et al. 2019). The expected SN Ia brightness is obtained by using the Hsiao template (Hsiao et al. 2007) with a peak B-band absolute magnitude of -19.26 mag (Richardson et al. 2014), which is an average absolute magnitude at peak. The SNe II includes SNe IIP, SNe IIL, and SNe IIn from the Nugent template[3]. The peak absolute magnitudes for SNe II are set as -18 mag in the V band in all the subtypes. The assumed SN II peak absolute magnitude is brighter than the average (Richardson et al. 2014), but the bright SNe II are preferentially discovered at high redshifts.

Figure 12 shows that high-redshift SNe Ia and SNe II can be as bright as high-redshift PISNe and SLSNe in the I_E band, but high-redshift SNe Ia and SNe II do not become as bright as high-redshift PISNe and SLSNe in the H_E band. Thus, the color between the I_E and H_E bands allows us to efficiently distinguish high-redshift PISNe and SLSNe from other SNe. While we do not assume any extinction in Fig. 12, the fact that SNe Ia and II are detected in the I_E band but not in the H_E band indicate their detections.

Host galaxy information of transients is also an important clue to identifying their redshift information. The reference

Figure 12 shows the color-magnitude diagrams in the I_E and H_E bands for RSG PISNe at $z > 0.5$ (top), WR PISNe at $z > 0.5$ (middle), and SLSNe at $z > 0.5$ (bottom). Each point shows color and magnitude for a certain epoch, and all epochs in the models are presented in the figure. We also present the expected color and magnitude regions for SNe Ia and SNe II at $z > 0.5$, assuming that those at $z < 0.5$ can be discovered by optical transient surveys with, for example, Subaru/HSC,

---

[3] https://c3.lbl.gov/nugent/nugent_templates.html

Fig. 10. Cumulative redshift distributions of SLSNe discovered in the survey simulations. The total discovery numbers in the three EDFs are presented.
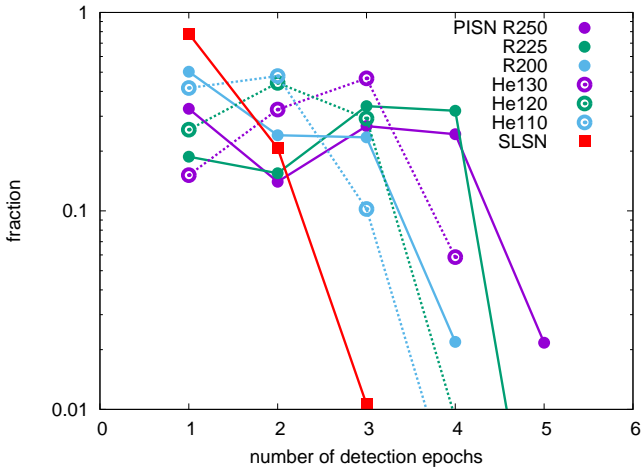
Fig. 11. Distribution of number of epochs for which luminous PISNe (R250, R225, R200, He130, He120, and He110) and SLSNe are detected with the EDFF cadence (Fig. 6). The distribution is obtained using the whole detected sample at all redshifts.

images taken at the beginning of EDS as well as deep optical images available in the EDFs would allow us to estimate host-galaxy photometric redshifts if the host galaxies are bright enough. Some host-galaxy spectra needed to determine their redshifts could be simultaneously obtained by the grisms on *Euclid*. The limiting magnitude of the reference images in the I_E band are around 26 mag or deeper. Therefore, host galaxies with absolute magnitudes brighter than around -19 mag in the rest-frame ultraviolet can be identified in the reference images. Many galaxies are fainter than -19 mag in the ultraviolet (e.g., Bouwens et al. 2021), and a large fraction of PISNe could be observed as hostless. Even if we have the host galaxy photometry, the photometric redshift estimates at high redshifts are challenging (e.g., Euclid Collaboration 2020). Despite the difficulties, host galaxy information provides additional clues that help identify the nature of transients. The NIR reference images will be shallower than that of I_E, but they can trace fainter stellar masses, and some host galaxies could only appear inside them.

Active galactic nuclei (AGNs) can be variable over long timescales and such a long-term AGN variability can contam-
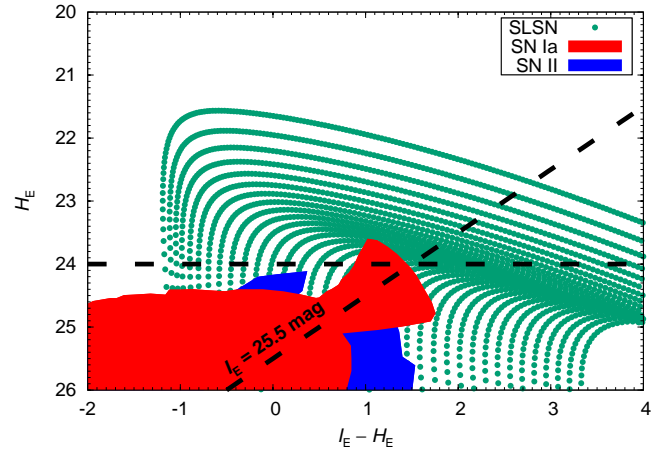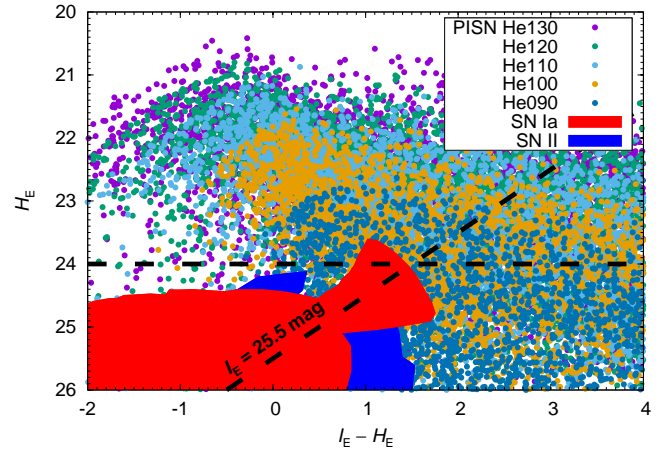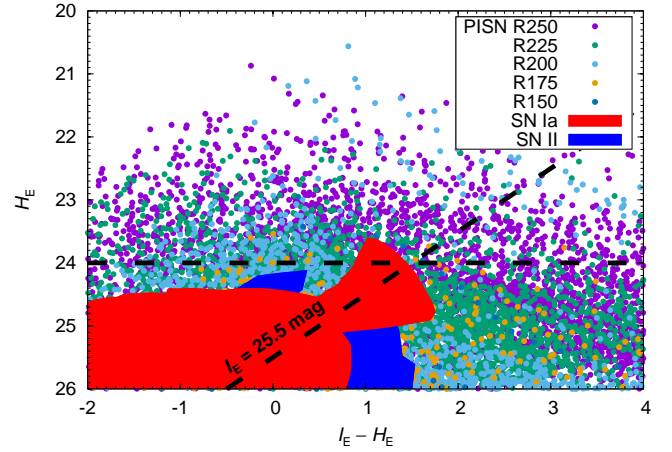
Fig. 12. Color–magnitude diagrams in the I_E and H_E bands for RSG PISNe (*top*), WR PISNe (*middle*), and SLSNe (*bottom*). PISNe and SLSNe at $z > 0.5$ at all phases are plotted with a redshift interval of 0.1. The color evolution with time can be found in Fig. 13. The regions covered by SNe Ia and SNe II at $z > 0.5$ are shown. No extinction is assumed. The survey limiting magnitudes for the I_E and H_E bands (25.5 mag and 24.0 mag in AB magnitudes, respectively) are indicated by the dashed lines. Most SNe Ia and SNe II at $z > 0.5$ are too faint to be detected in the H_E band with the 24.0 mag limit.

inate our sample of high-redshift PISN and SLSN candidates. The variable component of unobscured AGN spectra at ultraviolet to optical wavelengths is estimated to be proportional to $\nu^{1/3}$, where ν denotes the frequency (e.g., Kokubo et al. 2014). Thus,
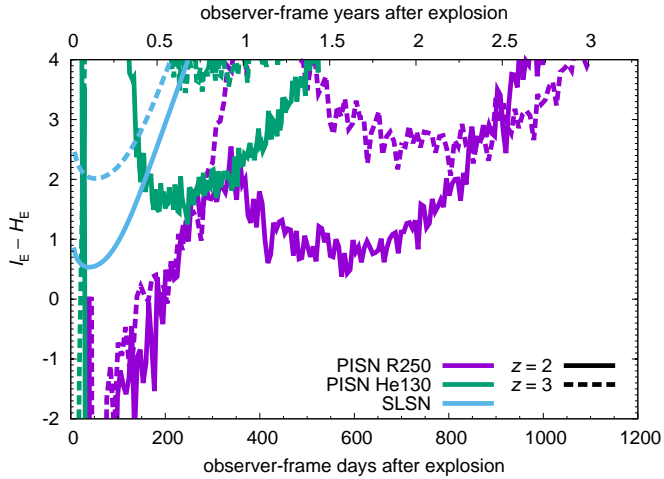
Fig. 13. Color evolution of the PISN models and SLSN template presented in Fig. 3.

the color of the AGN variability does not significantly change, and it remains at $I_E - H_E \simeq -0.34$ mag. Because the color of PISNe and SLSNe changes much more with time (Fig. 13), the color evolution is an essential piece of information to exclude AGN variability. In order to exclude AGNs with short-timescale variability, simultaneous short-cadence optical transient surveys are helpful. The location of transients in their host galaxies is also important to exclude AGNs, and the high spatial resolution of *Euclid* can help to constrain the nuclear versus nonnuclear location in host galaxies. Ultimately, spectroscopic confirmation of the transient would be required to confirm the classification as PISNe or SLSNe. It is possible that a part of the spectroscopic follow-up observations will be realized by the grisms on *Euclid*. The *James Webb* Space Telescope will also be powerful with regard to the spectroscopic follow-up observations. Photometric observations in narrower optical bands than I_E may also be useful to distinguish PISNe and SLSNe because of the different rest-frame ultraviolet properties expected in them (e.g., Dessart et al. 2012).

6. Conclusions

We estimated the expected number of PISN and SLSN discoveries in EDS, in which three EDFs (40 deg^2 in total) are planned to be observed regularly for six years during the *Euclid* mission. Although the EDF observations are not frequent (Fig. 6), the intrinsically long duration of PISNe and SLSNe allows us to discover them in the high-redshift Universe with the current survey plan. With the currently planned limiting magnitudes, it is possible to detect PISNe and SLSNe up to $z \simeq 3.5$ (Fig. 4). We find that we can discover up to several hundred PISNe with EDS if the bright PISN rate is as high as the SLSN rate (Table 2). The expected number of PISN discoveries exceeds unity as long as the bright PISN rate is higher than 1% of the SLSN rate. 30–120 SLSNe are expected to be discovered with the same survey, depending on the discovery criteria (Table 2). We also show that high-redshift PISN and SLSN candidates can be efficiently identified among abundant SNe such as SNe Ia using their duration, color, and magnitude (Figs. 2, 11, and 12).

The predicted total PISN rates are around 10–100% of the SLSN rate at $z \lesssim 3.5$ (Fig. 7). The bright PISNe that come from progenitor masses above $\simeq 200 M_\odot$ consist of about 50% of the entire PISN population, assuming a Salpeter initial mass func-

tion and a PISN progenitor mass range of 150–300 $M_\odot$. Even if we take 50% of the estimated number of discoveries from our survey simulations, our expected number of PISN discoveries exceed unity when the PISN rate is higher than 10% of the SLSN rate. Therefore, our study indicates that the *Euclid* mission provides an unprecedented opportunity to finally discover PISNe if the latest PISN rate predictions are accurate. If the PISN rate is sufficiently high, it is also possible that the *Euclid* mission will lead to the discovery of many PISNe with which PISNe in different environments and cosmic time can be studied. The identification and characterization of PISNe at $z \lesssim 3.5$ by the *Euclid* mission will allow us to directly confirm the existence of such objects that have never been identified with certainty before. The PISN properties can be compared with the theoretical predictions aimed at testing the theory of the evolution of massive stars in low-metallicity environments. They can also constrain massive star formation in the early Universe by providing the formation rate of the massive stars in the PISN mass range. The PISN discovery by the *Euclid* mission will be an important base to discover and characterize PISNe at higher redshifts ($z \gtrsim 3.5$), which can be reached by future missions such as the *Nancy Grace Roman* Space Telescope (e.g., Moriya et al. 2022; Lazar & Bromm 2022). Even if we do not discover any PISNe, we will be in a position to obtain a strong constraint on the PISN event rate at $z \lesssim 3.5$ that will challenge the current understanding of stellar evolution theory.

References

Aoki, W., Tominaga, N., Beers, T. C., Honda, S., & Lee, Y. S. 2014, Science, 345, 912
Astier, P., Balland, C., Brescia, M., et al. 2014, A&A, 572, A80
Barkat, Z., Rakavy, G., & Sack, N. 1967, Phys. Rev. Lett., 18, 379
Bouwens, R. J., Oesch, P. A., Stefanon, M., et al. 2021, AJ, 162, 47
Briel, M. M., Eldridge, J. J., Stanway, E. R., Stevance, H. F., & Chrimes, A. A. 2022, MNRAS, 514, 1315
Chatzopoulos, E., & Wheeler, J. C. 2012, ApJ, 748, 42
Chen, Z. H., Yan, L., Kangas, T., et al. 2022a, ApJ, submitted [arXiv:2202.02059]
Chen, Z. H., Yan, L., Kangas, T., et al. 2022b, ApJ, submitted [arXiv:2202.02060]
Chruslinska, M., & Nelemans, G. 2019, MNRAS, 488, 5300
De Cia, A., Gal-Yam, A., Rubin, A., et al. 2018, ApJ, 860, 100
Dessart, L., Hillier, D. J., Waldman, R., Livne, E., & Blondin, S. 2012, MNRAS, 426, L76
Dessart, L., Waldman, R., Livne, E., Hillier, D. J., & Blondin, S. 2013, MNRAS, 428, 3227
du Buisson, L., Marchant, P., Podsiadlowski, P., et al. 2020, MNRAS, 499, 5941
Eldridge, J. J., Stanway, E. R., Xiao, L., et al. 2017, PASA, 34, e058
Euclid Collaboration (Desprez, G., et al.) 2020, A&A, 644, A31
Euclid Collaboration (Scaramella, R., et al.) 2022a, A&A, 662, A112

Euclid Collaboration (Schirmer, M., et al.) 2022b, A&A, 662, A92
Farmer, R., Renzo, M., de Mink, S. E., Marchant, P., & Justham, S. 2019, ApJ, 887, 53
Fox, O. D., Khandrika, H., Rubin, D., et al. 2021, MNRAS, 506, 4199
Frohmaier, C., Angus, C. R., Vincenzi, M., et al. 2021, MNRAS, 500, 5142
Gal-Yam, A. 2019, ARA&A, 57, 305
Gal-Yam, A., Mazzali, P., Ofek, E. O., et al. 2009, Nature, 462, 624
Garn, T., & Best, P. N. 2010, MNRAS, 409, 421
Georgy, C., Meynet, G., Ekström, S., et al. 2017, A&A, 599, L5
Gilmer, M. S., Kozyreva, A., Hirschi, R., Fröhlich, C., & Yusof, N. 2017, ApJ, 846, 100
González-Gaitán, S., Tominaga, N., Molina, J., et al. 2015, MNRAS, 451, 2212
Guy, L. P., Cuillandre, J. C., Bachelet, E., et al. 2021, https://doi.org/10.5281/zenodo.5836022
Heger, A., & Woosley, S. E. 2002, ApJ, 567, 532
Hounsell, R., Scolnic, D., Foley, R. J., et al. 2018, ApJ, 867, 23
Hsiao, E. Y., Conley, A., Howell, D. A., et al. 2007, ApJ, 663, 1187
Inserra, C. 2019, Nat. Astron., 3, 697
Inserra, C., Nicholl, M., Chen, T. W., et al. 2017, MNRAS, 468, 4642
Inserra, C., Nichol, R. C., Scovacricchi, D., et al. 2018a, A&A, 609, A83
Inserra, C., Smartt, S. J., Gall, E. E. E., et al. 2018b, MNRAS, 475, 1046
Isobe, Y., Ouchi, M., Suzuki, A., et al. 2022, ApJ, 925, 111
Jencson, J. E., Kasliwal, M. M., Adams, S. M., et al. 2019, ApJ, 886, 40
Jerkstrand, A., Smartt, S. J., & Heger, A. 2016, MNRAS, 455, 3207
Kankare, E., Efstathiou, A., Kotak, R., et al. 2021, A&A, 649, A134
Kasen, D., Woosley, S. E., & Heger, A. 2011, ApJ, 734, 102
Kokubo, M., Morokuma, T., Minezaki, T., et al. 2014, ApJ, 783, 46
Kool, E. C., Ryder, S., Kankare, E., et al. 2018, MNRAS, 473, 5641
Kozyreva, A., Blinnikov, S., Langer, N., & Yoon, S. C. 2014, A&A, 565, A70
Langer, N. 2012, ARA&A, 50, 107
Langer, N., Norman, C. A., de Koter, A., et al. 2007, A&A, 475, L19
Laureijs, R., Amiaux, J., Arduini, S., et al. 2011, ArXiv e-prints [arXiv:1110.3193]
Lazar, A., & Bromm, V. 2022, MNRAS, 511, 2505
Lunnan, R., Chornock, R., Berger, E., et al. 2016, ApJ, 831, 144
Lunnan, R., Chornock, R., Berger, E., et al. 2018, ApJ, 852, 81
Madau, P., & Dickinson, M. 2014, ARA&A, 52, 415
Magg, M., Hartwig, T., Glover, S. C. O., Klessen, R. S., & Whalen, D. J. 2016, MNRAS, 462, 3591
Mannucci, F., Della Valle, M., & Panagia, N. 2007, MNRAS, 377, 1229
Marchant, P., Langer, N., Podsiadlowski, P., Tauris, T. M., & Moriya, T. J. 2016, A&A, 588, A50
Mattila, S., Dahlen, T., Efstathiou, A., et al. 2012, ApJ, 756, 111
Mazzali, P. A., Moriya, T. J., Tanaka, M., & Woosley, S. E. 2019, MNRAS, 484, 3451
Miller, A. A., Yao, Y., Bulla, M., et al. 2020, ApJ, 902, 47
Moriya, T. J., Sorokina, E. I., & Chevalier, R. A. 2018, Space Sci. Rev., 214, 59
Moriya, T. J., Wong, K. C., Koyama, Y., et al. 2019, PASJ, 71, 59
Moriya, T. J., Jiang, J.-A., Yasuda, N., et al. 2021, ApJ, 908, 249
Moriya, T. J., Quimby, R. M., & Robertson, B. E. 2022, ApJ, 925, 211
Nicholl, M. 2021, Astron. Geophys., 62, 34
Nicholl, M., Smartt, S. J., Jerkstrand, A., et al. 2013, Nature, 502, 346
Nicholl, M., Berger, E., Margutti, R., et al. 2017, ApJ, 835, L8
Nomoto, K., Kobayashi, C., & Tominaga, N. 2013, ARA&A, 51, 457
Pan, T., Kasen, D., & Loeb, A. 2012, MNRAS, 422, 2701
Pérez-Torres, M. A., Romero-Cañizales, C., Alberdi, A., & Polatidis, A. 2009, A&A, 507, L17
Perley, D. A., Fremling, C., Sollerman, J., et al. 2020, ApJ, 904, 35
Prajs, S., Sullivan, M., Smith, M., et al. 2017, MNRAS, 464, 3568
Quimby, R. M., Kulkarni, S. R., Kasliwal, M. M., et al. 2011, Nature, 474, 487
Quimby, R. M., Yuan, F., Akerlof, C., & Wheeler, J. C. 2013, MNRAS, 431, 912
Quimby, R. M., De Cia, A., Gal-Yam, A., et al. 2018, ApJ, 855, 2
Rakavy, G., & Shaviv, G. 1967, ApJ, 148, 803
Regős, E., Vinkó, J., & Ziegler, B. L. 2020, ApJ, 894, 94
Richardson, D., Jenkins, R. L., I, Wright, J., & Maddox, L. 2014, AJ, 147, 118
Scannapieco, E., Madau, P., Woosley, S., Heger, A., & Ferrara, A. 2005, ApJ, 633, 1031
Smith, N., Li, W., Foley, R. J., et al. 2007, ApJ, 666, 1116
Spergel, D., Gehrels, N., Baltay, C., et al. 2015, ArXiv e-prints [arXiv:1503.03757]
Stanway, E. R., & Eldridge, J. J. 2018, MNRAS, 479, 75
Steidel, C. C., Rudie, G. C., Strom, A. L., et al. 2014, ApJ, 795, 165
Strolger, L.-G., Dahlen, T., Rodney, S. A., et al. 2015, ApJ, 813, 93
Takahashi, K. 2018, ApJ, 863, 153
Tanikawa, A., Moriya, T. J., Tominaga, N., & Yoshida, N. 2022, ArXiv e-prints [arXiv:2204.09402]
Terreran, G., Pumo, M. L., Chen, T. W., et al. 2017, Nat. Astron., 1, 713
Vreeswijk, P. M., Savaglio, S., Gal-Yam, A., et al. 2014, ApJ, 797, 24
Whalen, D. J., Even, W., Frey, L. H., et al. 2013, ApJ, 777, 110
Wong, K. C., Moriya, T. J., Oguri, M., et al. 2019, PASJ, 71, 60
Yasuda, N., Tanaka, M., Tominaga, N., et al. 2019, PASJ, 71, 74

[1] National Astronomical Observatory of Japan, National Institutes of Natural Sciences, 2-21-1 Osawa, Mitaka, Tokyo 181-8588, Japan
[2] School of Physics and Astronomy, Faculty of Science, Monash University, Clayton, Victoria 3800, Australia
[3] School of Physics and Astronomy, Cardiff University, The Parade, Cardiff CF24 3AA, UK
[4] Astronomical Institute, Tohoku University, Sendai 980-8578, Japan
[5] Division for the Establishment of Frontier Sciences, Organization for Advanced Studies, Tohoku University, Sendai 980-8577, Japan
[6] INAF-Osservatorio Astronomico di Padova, Via dell'Osservatorio 5, 35122 Padova, Italy
[7] INAF-Osservatorio Astronomico di Capodimonte, Via Moiariello 16, 80131 Napoli, Italy
[8] INFN section of Naples, Via Cinthia 6, 80126 Napoli, Italy
[9] International Center for Relativistic Astrophysics, Piazzale della Republica 2, 65122 Pescara, Italy
[10] Department of Physics, Lancaster University, Lancaster LA1 4YB, UK
[11] Department of Physics and Astronomy, University of Turku, Vesilinnantie 5, 20014 Turku, Finland
[12] Department of Physics "E. Pancini", University Federico II, Via Cinthia 6, 80126 Napoli, Italy
[13] INAF-Osservatorio Astrofisico di Arcetri, Largo E. Fermi 5, 50125 Firenze, Italy
[14] Aix-Marseille Univ, CNRS/IN2P3, CPPM, Marseille, France
[15] ESAC/ESA, Camino Bajo del Castillo, s/n., Urb. Villafranca del Castillo, 28692 Villanueva de la Cañada, Madrid, Spain
[16] Institute of Cosmology and Gravitation, University of Portsmouth, Portsmouth PO1 3FX, UK
[17] INAF-Osservatorio di Astrofisica e Scienza dello Spazio di Bologna, Via Piero Gobetti 93/3, 40129 Bologna, Italy
[18] INAF-Osservatorio Astrofisico di Torino, Via Osservatorio 20, 10025 Pino Torinese, TO, Italy
[19] INFN-Sezione di Roma Tre, Via della Vasca Navale 84, 00146 Roma, Italy
[20] Dipartimento di Fisica, Universitá degli studi di Genova, and INFN-Sezione di Genova, Via Dodecaneso 33, 16146 Genova, Italy
[21] Instituto de Astrofísica e Ciências do Espaço, Universidade do Porto, CAUP, Rua das Estrelas, 4150-762 Porto, Portugal
[22] Dipartimento di Fisica, Universitá degli Studi di Torino, Via P. Giuria 1, 10125 Torino, Italy
[23] INFN-Sezione di Torino, Via P. Giuria 1, 10125 Torino, Italy
[24] INAF-IASF Milano, Via Alfonso Corti 12, 20133 Milano, Italy
[25] Port d'Informació Científica, Campus UAB, C. Albareda s/n, 08193 Bellaterra, Barcelona, Spain
[26] Institut de Física d'Altes Energies (IFAE), The Barcelona Institute of Science and Technology, Campus UAB, 08193 Bellaterra, Barcelona, Spain
[27] INAF-Osservatorio Astronomico di Roma, Via Frascati 33, 00078 Monteporzio Catone, Italy
[28] Dipartimento di Fisica e Astronomia "Augusto Righi" – Alma Mater Studiorum Università di Bologna, Via Piero Gobetti 93/2, 40129 Bologna, Italy
[29] Institut National de Physique Nucléaire et de Physique des Particules, 3 rue Michel-Ange, 75794 Paris Cedex 16, France
[30] Centre National d'Etudes Spatiales, Toulouse, France
[31] Institute for Astronomy, University of Edinburgh, Royal Observatory, Blackford Hill, Edinburgh EH9 3HJ, UK
[32] Jodrell Bank Centre for Astrophysics, Department of Physics and Astronomy, University of Manchester, Oxford Road, Manchester M13 9PL, UK
[33] European Space Agency/ESRIN, Largo Galileo Galilei 1, 00044 Frascati, Roma, Italy
[34] Univ Lyon, Univ Claude Bernard Lyon 1, CNRS/IN2P3, IP2I Lyon, UMR 5822, 69622 Villeurbanne, France

[35] Institute of Physics, Laboratory of Astrophysics, Ecole Polytechnique Fédérale de Lausanne (EPFL), Observatoire de Sauverny 1290 Versoix, Switzerland

[36] Mullard Space Science Laboratory, University College London, Holmbury St Mary, Dorking, Surrey RH5 6NT, UK

[37] Departamento de Física, Faculdade de Ciências, Universidade de Lisboa, Edifício C8, Campo Grande, 1749-016 Lisboa, Portugal

[38] Instituto de Astrofísica e Ciências do Espaço, Faculdade de Ciências, Universidade de Lisboa, Campo Grande, 1749-016 Lisboa, Portugal

[39] Department of Astronomy, University of Geneva, ch. dÉcogia 16, 1290 Versoix, Switzerland

[40] Université Paris-Saclay, CNRS, Institut d'astrophysique spatiale, 91405 Orsay, France

[41] Department of Physics, Oxford University, Keble Road, Oxford OX1 3RH, UK

[42] INFN-Padova, Via Marzolo 8, 35131 Padova, Italy

[43] Université Paris-Saclay, Université Paris Cité, CEA, CNRS, Astrophysique, Instrumentation et Modélisation Paris-Saclay, 91191 Gif-sur-Yvette, France

[44] INAF-Osservatorio Astronomico di Trieste, Via G. B. Tiepolo 11, 34143 Trieste, Italy

[45] Istituto Nazionale di Astrofisica (INAF) – Osservatorio di Astrofisica e Scienza dello Spazio (OAS), Via Gobetti 93/3, 40127 Bologna, Italy

[46] Istituto Nazionale di Fisica Nucleare, Sezione di Bologna, Via Irnerio 46, 40126 Bologna, Italy

[47] Max Planck Institute for Extraterrestrial Physics, Giessenbachstr. 1, 85748 Garching, Germany

[48] Universitäts-Sternwarte München, Fakultät für Physik, Ludwig-Maximilians-Universität München, Scheinerstrasse 1, 81679 München, Germany

[49] Institute of Theoretical Astrophysics, University of Oslo, PO Box 1029 Blindern, 0315 Oslo, Norway

[50] Jet Propulsion Laboratory, California Institute of Technology, 4800 Oak Grove Drive, Pasadena, CA 91109, USA

[51] von Hoerner & Sulger GmbH, Schloßplatz 8, 68723 Schwetzingen, Germany

[52] Technical University of Denmark, Elektrovej 327, 2800 Kgs. Lyngby, Denmark

[53] Max-Planck-Institut für Astronomie, Königstuhl 17, 69117 Heidelberg, Germany

[54] Department of Physics and Helsinki Institute of Physics, Gustaf Hällströmin katu 2, 00014 University of Helsinki, Finland

[55] NOVA Optical Infrared Instrumentation Group at ASTRON, Oude Hoogeveensedijk 4, 7991PD Dwingeloo, The Netherlands

[56] Argelander-Institut für Astronomie, Universität Bonn, Auf dem Hügel 71, 53121 Bonn, Germany

[57] INFN-Sezione di Bologna, Viale Berti Pichat 6/2, 40127 Bologna, Italy

[58] Department of Physics, Institute for Computational Cosmology, Durham University, South Road, DH1 3LE, UK

[59] Institut d'Astrophysique de Paris, UMR 7095, CNRS, and Sorbonne Université, 98 bis boulevard Arago, 75014 Paris, France

[60] University of Applied Sciences and Arts of Northwestern Switzerland, School of Engineering, 5210 Windisch, Switzerland

[61] European Space Agency/ESTEC, Keplerlaan 1, 2201 AZ Noordwijk, The Netherlands

[62] Department of Physics and Astronomy, University of Aarhus, Ny Munkegade 120, 8000 Aarhus C, Denmark

[63] Institute of Space Science, Bucharest 077125, Romania

[64] IFPU, Institute for Fundamental Physics of the Universe, Via Beirut 2, 34151 Trieste, Italy

[65] Dipartimento di Fisica e Astronomia "G. Galilei", Universitá di Padova, Via Marzolo 8, 35131 Padova, Italy

[66] Centro de Investigaciones Energéticas, Medioambientales y Tecnológicas (CIEMAT), Avenida Complutense 40, 28040 Madrid, Spain

[67] Instituto de Astrofísica e Ciências do Espaço, Faculdade de Ciências, Universidade de Lisboa, Tapada da Ajuda, 1349-018 Lisboa, Portugal

[68] Universidad Politécnica de Cartagena, Departamento de Electrónica y Tecnología de Computadoras, 30202 Cartagena, Spain

[69] Infrared Processing and Analysis Center, California Institute of Technology, Pasadena, CA 91125, USA

[70] INAF-Osservatorio Astronomico di Brera, Via Brera 28, 20122 Milano, Italy

[71] Junia, EPA Department, 59000 Lille, France

[72] California institute of Technology, 1200 E California Blvd, Pasadena, CA 91125, USA